The Siberian Solar Radio Telescope: the current state of the instrument, observations, and data

V.V. Grechnev, S.V. Lesovoi, G.Ya. Smolkov, B.B. Krissinel, V.G. Zandanov, A.T. Altyntsev, N.N. Kardapolova, R.Y. Sergeev, A.M. Uralov, V.P. Maksimov and B.I. Lubyshev
Institute of Solar-Terrestrial Physics, P.O. Box 4026, Lermontov Street 126, Irkutsk 664033, Russia

Abstract.

The Siberian Solar Radio Telescope is one of the World's largest solar radio heliographs. It commenced operation in 1983, and since then has undergone several upgrades. The operating frequency of the SSRT is 5.7 GHz. Since 1992 the instrument has had the capability to make one-dimensional scans with a high time resolution of 56 ms and an angular resolution of 15 arcsec. Making one of these scans now takes 14 ms. In 1996 the capability was added to make full, two-dimensional images of the solar disk. The SSRT is now capable of obtaining images with an angular resolution of 21 arcsec, every two minutes. In this paper we describe the main features and operation of the instrument, particularly emphasizing issues pertaining to the imaging process and factors limiting data quality. Some of the data processing and analysis techniques are discussed. We present examples of full-disk solar images of the quiet sun, recorded near solar activity minimum, and images of specific structures: plages, coronal bright points, filaments and prominences, and coronal holes. We also present some observations of dynamic phenomena, such as eruptive prominences and solar flares, which illustrate the high time resolution observations that can be done with this instrument. We compare SSRT observations at 5.7 GHz, including computed 'light curves', with observations, such as 17 GHz radio images, Hα filtergrams and magnetograms, extreme-ultraviolet and X-ray observations, and dynamic radio spectra.

1. Introduction

The Siberian Solar Radio Telescope is one of the World's largest radio heliographs. It is dedicated exclusively to solar observations and has been operating for two decades. The working frequency is 5.7 GHz. Solar radio emissions at this frequency originate primarily in the solar corona, with a probable contribution from the transition region, both on the solar disk and above the limb. An extensive data archive containing one- and two-dimensional observations has been accumulated to date. A brief description of the SSRT was given by Smolkov *et al.* (1986). Since that time, during the last solar cycle, the SSRT underwent several upgrades, during which new observing modes were implemented. This was achieved without any interruption to the observations. It is therefore timely to describe the upgraded capabilities of the instrument, the

observational data being produced, and the instrumental limitations to data quality.

The magnetic field strengths in the corona overlying sunspots are such that gyroresonant absorption at low harmonics of the electron gyrofrequency leads to large optical thicknesses in frequencies in the range 3–5 GHz. This leads to active region emission standing out with high contrast against the background disk emission, which is due to free-free, thermal processes. High sensitivity, high-resolution intensity and polarization observations of gyroresonance and free-free emissions provide a powerful means by which the structure and dynamics of coronal magnetic fields may be studied (Felli, Lang, and Willson, 1981; Kundu 1985).

Another design objective of the SSRT was the high time-resolution observation of solar radio bursts at 5.7 GHz. One-dimensional observations can be made with a time resolution of 0.2 s and an angular resolution of up to $15''$. Two-dimensional images can be made with the rather poorer angular resolution of $21''$, and the much lower time resolution of one image every 2 minutes. These limitations are set by the technologies available in the 1970's when the project was started. High-resolution solar mapping at centimeter wavelengths has been carried out using large interferometers such as Very Large Array (VLA; Napier *et al.*, 1983) and Westerbork Synthesis Radio Telescope (WSRT; Baars and Hooghoudt, 1974). However, the VLA and WSRT are not dedicated exclusively to making solar observations, so, although their angular resolution is better than available using other instruments, such as the SSRT, their availability is lower, and many interesting events may be missed. The SSRT is used exclusively for making solar observations, and so offers almost complete time coverage for as long as the Sun is above the horizon. It may therefore be more effective for studies of dynamics and evolutionary change in active region structures.

Linear arrays, such as the WSRT and the Synthesis Radio Telescope at DRAO (Landecker *et al.*, 2000; Tapping, Cameron, and Willis, 2003) require twelve hours to collect the information needed to obtain a complete, two-dimensional image; the SSRT, having a two-dimensional antenna array, can obtain a full, two-dimensional image, in two to three minutes. The SSRT has the disadvantage of poorer angular resolution, so that only larger structures may be mapped. However, the available angular resolution, in combination with the short mapping time (a complete, two-dimensional image every three minutes) and the large mapping field, which permits mapping the whole solar disk in a single operation, makes this instrument suitable for studies of active region emissions as contributions to the global slowly-varying component (Zubkova *et al.*, 1990; Nefedyev *et al.*, 1993; Maksimov and Bakunina,

1991, 1995, 1996). The dynamic range of the SSRT allows observing the low-contrast features simultaneously with observations of bright sources in active regions.

In the course of construction and during observations, the time resolution and sensitivity of the SSRT have been substantially improved, thus extending the range of the physical tasks that can be solved using observations at the SSRT. The receiver upgrades in the early 1990's made it possible to study fine time structures in 5.7 GHz emissions from transient events. The fine time structure of radio bursts in the 5.7 GHz frequency range can be a powerful tool in the identification of the relevant dynamic and plasma processes in the source. On the other hand, it is difficult to identify them without information about the localization and other spatial characteristics of the emitting sources. When one-dimensional observations with high time resolution started at the SSRT, only few other spatially resolved observations of fine time structures were available. The observations of subsecond-timescale impulsive centimetric emission with one-dimensional resolution carried out since 1992 are actually a unique contribution of the SSRT. Second, improvement of the sensitivity due to several upgrades of the low-noise amplifiers in the SSRT waveguide system made it also possible to study features of relatively low contrast with respect to the solar disk.

The SSRT currently observes the quiet Sun, filaments and prominences, coronal holes and bright points, features in active regions such as plages, sunspot-associated sources and neutral line-associated sources.

For solar stidues it is important that solar observations are carried out at three frequencies, 5.7, 17, and 34 GHz at two large radioheliographs, the SSRT and Nobeyama Radioheliograph (NoRH, Nakajima et al., 1994), with almost full overlapping of the observational daytimes. The data acquired at these three frequencies supply information about coronal processes an different heights in the corona and give an opportunity to estimate the contribution of various radio emission mechanisms.

In this paper, the current state of the SSRT is presented, mainly from the viewpoint of the acquired data and its observational capabilities. We discuss its observing modes, major characteristics, and data types for different periods of the observations. We want to show both the advantages and limitations of the SSRT observations to make its data comprehensible for the solar community. The instrumentation and the imaging technique at the SSRT are briefly described in Section 1. We overview SSRT data as well as the observing modes and characteristics of the instrument for different years in Section 2. Some examples of quiet Sun observations are presented in Section 3. Examples of SSRT observations of dynamic phenomena are shown in Section 4.

Figure 1. View of the antenna system.

2. The instrument

The SSRT is located at Badary in the Tunka valley in Eastern Siberia, 220 km from Irkutsk. Its geographic coordinates are N 51°45′, E 102°13′. The SSRT is a cross-shaped interferometer consisting of two equidistant linear arrays, EW and NS, each of $N = 128$ antennas spaced by $d = 4.9$ m (Fig. 1 and 2). Each interferometer's baseline is 622.3 m. Cassegrain antennas with a diameter of 2.5 m and a focal length of 75 cm are mounted equatorially, which determines very simple algorithms of the antenna pointing control system. The working frequency $\nu_0 = 5.73$ GHz ($\lambda = 5.2$ cm, the frequency band from 5.67 to 5.79 GHz). The antennas detect left- and right-handed circularly polarized radiation (LCP and RCP). The feed of each antenna is equipped with a ferrite polarization modulator. The period of polarization modulation is 14 ms. At present, the SSRT observes the Sun in the two-dimensional mode with a spatial resolution of up to 21″, and in the one-dimensional mode with a spatial resolution of up to 15″.

Imaging is performed using the dependence of the angular position of an interference maximum (order) on the observing frequency (*frequency scanning*) and using the diurnal rotation of the Earth. The frequency scanning is not widely used in radio astronomy; hence we briefly explain this method.

The response of a two-element interferometer with a baseline d to a point source, which has a flat frequency spectrum, is a cosine depending on both the observing direction θ and the operating frequency ν:

$$F(\theta, \nu) \propto 1 + \cos\left(\frac{2\pi d\nu}{c}\cos\theta\right)$$

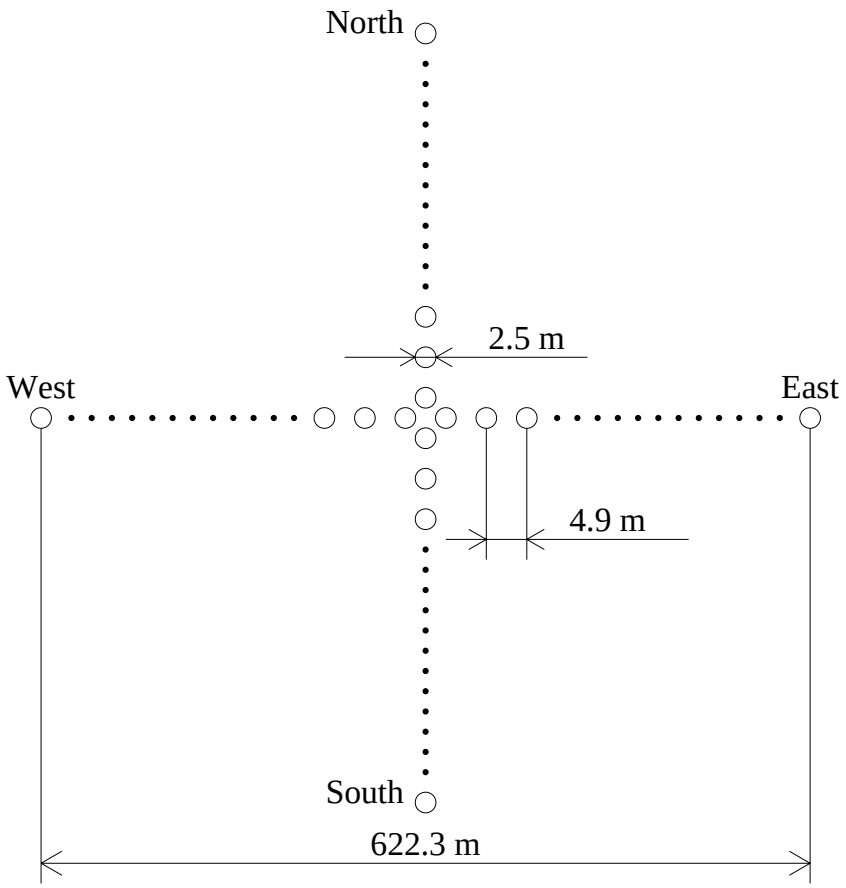

Figure 2. Diagram of the antenna system.

with c being the speed of light. Because the response is a periodic function, there exist maxima of the response, *interference maxima*, depending on the observing direction and frequency. They are determined by the expression $\cos\theta_n = nc/(\nu d)$, with numbers $n = 0, \pm 1, \ldots, \pm n_{\max}$, and occur in the directions θ_n relative to the interferometer baseline. These maxima are characterized by corresponding distances and widths in both the frequency and spatial domains.

In a small vicinity $\Delta\theta$ of the observing direction θ, this expression can be transformed:

$$F\left(\theta, \Delta\theta, \nu\right) \propto 1 + \cos\left(\Omega_\nu\left(d, \theta\right)\nu - \Psi_\nu\left(\Delta\theta\right)\right)$$

with $\Omega_\nu = \frac{\pi d}{c}\sin\theta$, $\Psi_\nu = \frac{\pi d \nu_0}{c}\cos\theta$.

In modelling the performance of a multi-element interferometer, the instrument can be treated as a large number of two-element interfer-

ometers. The frequency response of the array is therefore given by the sum of the frequency responses of each antenna pair, considered as a two-element interferometer. If a compact source with a flat frequency spectrum is observed in the direction θ, the multi-element linear interferometer synthesizes its one-dimensional image in the frequency domain. Because the response is a periodic function in the frequency domain, it can contain more than one image of the same source. This is determined by the condition $c/\left(d\cos\theta\right) < \Delta\nu$, with $\Delta\nu$ being the operating bandwidth of the SSRT.

The response of the interferometer in the spatial domain is also periodic. To exclude the mixture of responses from different interference orders, the angular size of the observed object $\Delta\Theta$ must not be large, $\Delta\Theta < \lambda/\left(d\sin\theta\right)$. The fundamental spacing of the SSRT, d, meets this condition for the Sun. The angular resolution of the interferometer is determined by the longest baseline $\rho_\theta = \lambda/\left(N d\sin\theta\right)$.

The characteristics of two-dimensional and one-dimensional data produced with the SSRT differ due to the different parameters of the corresponding beams. A total number of two-dimensional images produced by the SSRT is determined by the amount of intersections of the interference orders of the interferometers NS and EW only (for each interferometer, $n_{max} = \nu d/c = 93$) and depends on the observational day alone. The rate at which the one-dimensional data are produced by the instrument depends on sampling interval. The ultimate limiting factor on data rate is the response time of the polarization modulators. The side lobe levels are also different for two- and one-dimensional beams. Two-dimensional SSRT beam in a small vicinity $\Delta\theta < N/u_n$, $\Delta\eta < N/v_m$ of the interference orders $[\theta_n, \eta_m]$ can be represented as

$$F_{2D}\left(\Delta\theta, \Delta\eta\right) \propto (-1)^{n+m} \frac{\sin(\pi u_n \Delta\theta)}{\pi u_n \Delta\theta} \frac{\sin(\pi v_m \Delta\eta)}{\pi v_m \Delta\eta},$$

with $u_n = N d\sin\theta_n/\lambda$ and $v_m = N d\sin\eta_m/\lambda$ being the highest spatial harmonics of the linear interferometers. The side lobe level falls off with its number k as $(2k+1)^{-1}$, and the maximum level amounts to 22% of the main maximum. The relatively low level of the side lobes allows using two-dimensional maps without corrections for sampling or calibration problems when the brightness of radio sources is moderate. For the one-dimensional beam

$$F_{1D}\left(\Delta\theta\right) \propto \left(\frac{\sin(\pi u_n \Delta\theta)}{\pi u_n \Delta\theta}\right)^2,$$

the side lobe level falls off with its number as $(2k+1)^{-2}$, and the maximum level is 5% of the main maximum. We do not clean one-dimensional data because of the low level of the side lobes.

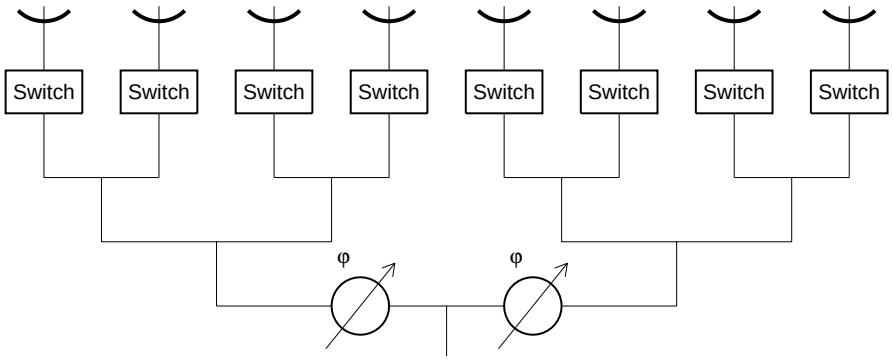

Figure 3. Block diagram of the SHF signal acquisition waveguide system.

2.1. Signal acquisition

The signals from each antenna come into the waveguide system through the controllable superhigh frequency (SHF) switches (Figure 3) that allow individual selection of each antenna in testing modes. Then the signals from all antennas are combined using the waveguide system. The system has a structure of a binary tree to make the electrical lengths from all antennas equal. The 4^{th} to 128^{th} nodes of the waveguide system have variable phase shifters that are capable of adding additional phase delays ranging from 0 to 360°. The standard deviation of the phase alignment is currently about 8°[1]. Output signals are combined in each node of the binary-tree waveguide system. Amplifiers with a noise temperature of 60 K are installed in nodes after each group of 16 antennas. The outputs from each of the four arms are combined to form NS and EW output signals.

The waveguide system is arranged in an underground tunnel to reduce the phase instability due to temperature variations. Remotely-controlled peripheral subsystems are located in the nodes of 16 antennas of the SSRT.

2.2. Receiving systems

A well-known modulation technique is used to extract the correlation component. The phases of the output signals of the two linear interferometers NS and EW are modulated in the cross point of the tunnel. The signals are combined into in-phase and anti-phase sums. The modulated signal comes to the frequency converter located in the observation building.

[1] The redundancy of the spatial spectrum in the one-dimensional mode significantly reduces the sensitivity of the response to the amplitude and phase distortions.

The frequency scanning is implemented at the SSRT through the recording power spectrum of the signal from the output of the interferometer, hence, the principal part of the receiving system is a spectrum analyzer of the intermediate-frequency signal. Historically, there are two spectrum-analyzing systems of parallel analysis. Both of them are superheterodyne receivers. One is an initial 180-channel multi-frequency filter bank (MFB) developed in the course of the SSRT construction. The other is an acoustic-optical spectrum analyzer (AOR) built in early nineties. The present AOR has 500 channels. Each of the receiving systems operates independently.

The block diagram of the receiving system of the SSRT is shown in Figure 4. Basically, the structure of both the MFB and AOR receivers is the same. The mixer combines signals from a high-stability oscillator (*Osc*) with amplified signals from the waveguide system. Then the amplified intermediate-frequency (IF) signals are led to the spectrum analyzer, AOR (IF = 210 MHz) or MFB (IF = 70 MHz). The sampling interval of the data acquisition system is currently 7 ms. Individual samples are summed up by the computer of the data acquisition system to form averaged samples with a period of 336 ms and recorded into the hard disk. The 14-ms time resolution data are only saved for fine time structured events. Raw data files are stored at CD-R's.

The summation of all antenna signals in the waveguide system determines a very high dynamic range of input signals, which is a critical point of a directly imaging telescope, thus requiring a controllable attenuator. A 21-dB attenuator is controlled by the data acquisition system using real-time analysis of signal levels.

The receiving system is connected to the other systems of the SSRT by means of a local area network (*LAN*) using the TCP/IP protocol. The clock system uses GPS signals. The timing accuracy is 1 ms.

2.3. Imaging

Unlike synthesizing interferometers (e.g., NoRH), SSRT is a directly imaging instrument and does not use the aperture synthesis technique. The dependence of the angular position of an interference maximum on the observing frequency is used to scan the Sun in altitude. The working frequency range of the SSRT of 5.67 to 5.79 GHz is practically always sufficient to cover the whole solar disk. The Sun is scanned in another direction (in hour angle) due to the diurnal rotation of the Earth. Therefore, one image of the Sun (a standard frame of $42' \times 42'$) is formed in about three minutes. The typical interval between successive two-dimensional images is about 2 minutes.

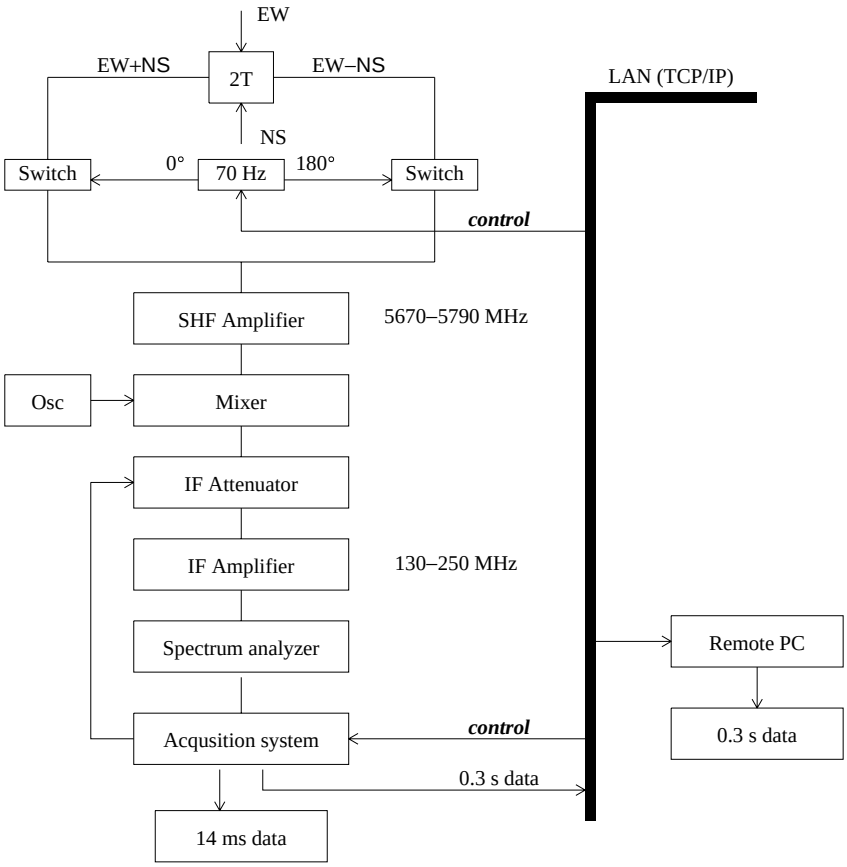

Figure 4. Block diagram of the receiver system.

The imaging process at the SSRT is illustrated with Figure 5 where a part of a raw record is shown (13 August 2002). Initially, the output signals of the two linear interferometers NS and EW are combined in in-phase and anti-phase sums (Fig. 5a and 5b) using the modulation technique. After the detection, the corresponding sums are subtracted from each other to form the correlation component (Fig. 5c). Two upper panels show in-phase and anti-phase sums, and the lower panel shows the correlation component. Each sample (vertical cross section in the Figure) of the raw record is a sum of one-dimensional spatial profiles of the Sun recorded with the EW and NS arrays according to their current scanning directions.

The responses obtained from the pass of successive interference orders (for each linear interferometer) have alternate signs, and the dark and light ellipses in Fig. 5c are the corresponding images of the solar

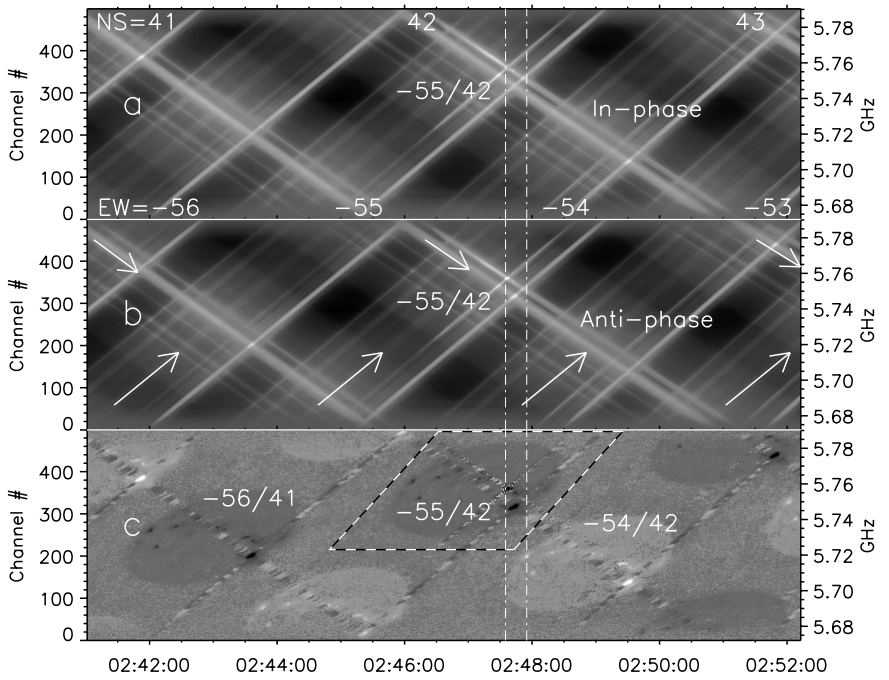

Figure 5. A part of a raw record (13 August 2002): a) in-phase sum, b) anti-phase sum, c) correlation component computed through the subtraction of the initial in-phase and anti-phase sums. Numbers in the upper panel show interference orders passed by the *EW* and *NS* interferometers, and in the lower panel they show solar images formed in passes of the Sun through the corresponding pairs of the *EW* and *NS* interference maxima. A rhombus in the lower panel shows the projection of a square-shaped area on the sky from which a standard frame of $42' \times 42'$ is formed. Two vertical lines mark a short time interval of 20 s for which the time profiles are shown in Figure 16. All images are nonlinearly processed to make both bright sources and the quiet Sun pronounced.

disk. A rhombus in the lower panel shows the projection of a square-shaped area on the plane of the image from which the standard frame of $42' \times 42'$ is formed in the pass of the Sun through the intersection of the 55-th *EW* order with the 42-nd *NS* order. An impulsive short-duration burst occurred during this pass, so that its image is visible during this pass only. The time profiles of this short burst are shown in Figure 16 within a short time interval of 20 s marked by two vertical dash-dotted lines.

Bright slanted strips in the in-phase and anti-phase sums are traces of bright, relatively stable radio sources recorded with the *EW* and *NS* linear interferometers. The arrows in the middle panel show the direction corresponding to the *EW* interference orders −56 through

-53 (below) and to the NS orders $+41$ through $+43$ (above). The slopes vary during a day depending on the directions θ_n with respect to the baselines of each linear interferometer.

The figure also illustrates the formation of one-dimensional data simultaneously with two-dimensional imaging. This example shows the present situation (starting from 2000), i.e., the outputs from EW and NS linear interferometers are combined. Using independent recordings of the output signals of the two linear interferometers, high-time-resolution unmixed one-dimensional images of the Sun were obtained in 1993-2000 (Altyntsev *et al.* 1996b) to form two spatial profiles in two directions. The independent recording from the two linear interferometers is currently not available, and we plan to resume it next year.

We can see some features of the SSRT imaging from Figure 5. First, the slanted strips corresponding to traces of bright sources observed in subsequent interference orders of EW interferometer obviously overlap with each other, i.e., the same source is observed in two different frequency channels simultaneously. However, there are gaps in the one-dimensional record from the NS interferometer in the intervals 02:45:30–02:46:00 and 02:50:45–02:51:15 (Fig. 5a, b). The presence of these gaps or overlapping depends on the observing directions $\theta_{n,m}$. These gaps occur at different times for each linear interferometer. As a result, a continuous source flux time profile can be computed.

Next, depending on the observing direction relative to the baselines, the SSRT can simultaneously observe the Sun in two interference orders at different frequencies within the operating bandwidth, as seen in Figure 5. This feature gives an opportunity to estimate the spectral slope of the emission under these conditions (Altyntsev *et al.*, 1996a).

The distance between adjacent interference orders virtually determines the field of view. It varies depending on the solar position relative to the SSRT baselines. Under favorable conditions, this allows erupting prominences to be observed up to heights of three solar radii from the solar disk center.

Figure 6 shows solar maps produced from the raw data. The maps have been formed from the pass of the Sun across the interference maxima $-56/41$ (the impulsive source is observed in the pass of $-55/42$). 'Dirty' solar maps (Fig. 6a) are constructed from the raw data using geometrical transformations to correct projection warping[2]. Because the sidelobe level of the SSRT beam pattern is relatively low (≤ 22 %

[2] 'Dirty image' is the image as output from the imaging process. It has not been corrected for sampling or calibration problems. 'Clean image' is the image after application of an algorithm to correct the above. In general this term is applied to an image to which the CLEAN algorithm has been applied.

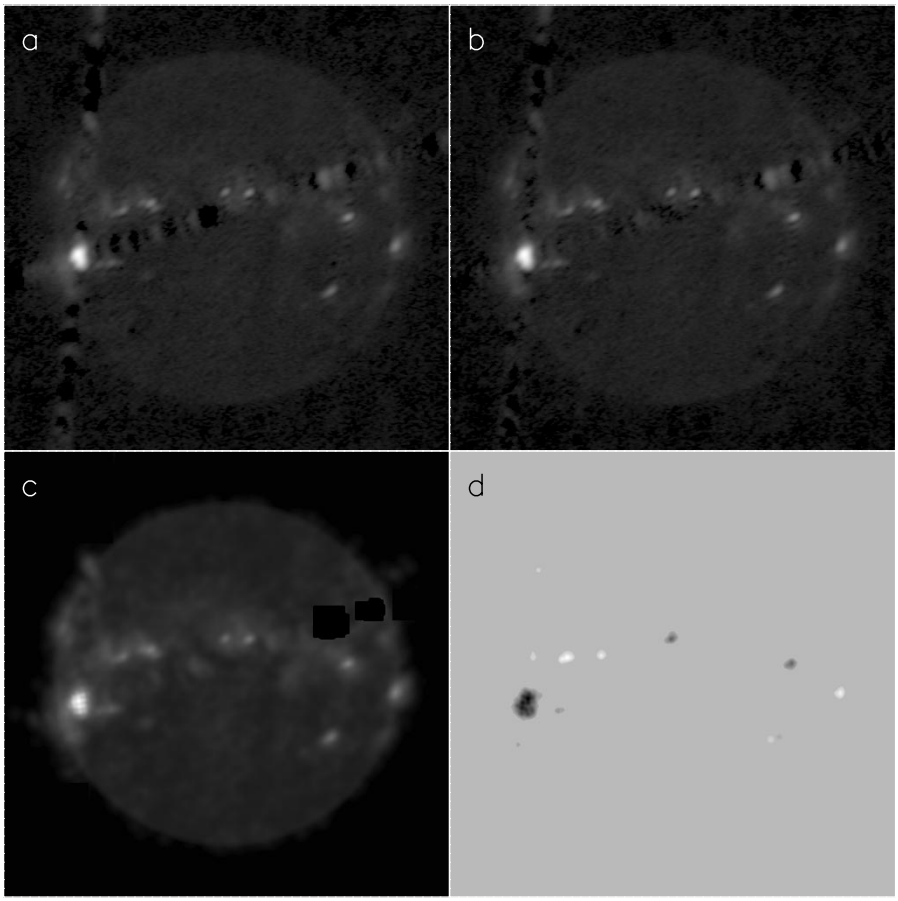

Figure 6. Solar Stokes I (a-c) and V (d) maps produced from the raw record (shown in Fig. 5, 13 August 2002). a, projection-corrected dirty map; b, beam-corrected map; c and d, clean maps. All images are nonlinearly processed to make both bright sources and the quiet Sun pronounced. Regions where the clean gave no satisfactory results are filled in with black.

for a point-like source), it is even possible to use dirty maps when radio sources on the Sun are not very bright (Uralov *et al.* 1998). Insufficiently accurate knowledge of the spectrum analyzer characteristics results in some geometrical distortions of images. The non-uniformity of the spectrum analyzer characteristics also causes some additional one-dimensional variations of the brightness temperature across the solar disk.

Figure 6b shows a beam-corrected map produced from the dirty map. By means of an iterative analysis of the dirty map, we infer distortions of the beam pattern due to the amplitude and phase errors in the antenna and waveguide systems of the SSRT. Then the dirty map

is corrected using inverse filtering with the estimated approximation of the real beam pattern. We can see the limitation of this method in Fig. 6b, i.e., the far side lobes with numbers exceeding 50–55 do not fall away.

Then a performance-optimized CLEAN algorithm is applied to the maps. The optimization concerns two points: (1) the search for the current maximum in a source image is optimized by means of the search within a floating window, which is small relative to the size of the whole image, and (2) the shift of the beam is optimized by means of amplitude filtering of the number of significant points in the array of the beam. The algorithm is also adapted for reconstructing extended sources, i.e., the convolution of an ideal beam pattern with model sources of various sizes is used as a clean beam. The present accuracy of the phase measurements of the antenna-waveguide system does not permit us to perform high-quality deconvolution of low-contrast features automatically. We have not yet developed a robust algorithm to infer the beam shape from observations. Therefore, intervention of a user is required in preparation of the dirty beam for the CLEAN routine, which is time and effort consuming. Clean maps are shown in Figure 6c (Stokes I) and 6d (Stokes V). Regions where the CLEAN routine gave no satisfactory results are filled in with black in Stokes I map (NW quadrant in Fig. 6c).

We calibrate the Stokes I and V images as $I = (RCP+LCP)/2$ and $V = (RCP - LCP)/2$, respectively, adopting the quiet Sun's brightness temperature $T_{QS} = 16\,000$ K (Zirin, Baumert, and Hurford, 1991; Borovik 1994). In particular, the maximum brightness temperature in the image shown in Fig. 6 is 2.7 MK. The overall sensitivity in solar observations is currently 1 500 K for an image formed in a single pass of the Sun (integration time 0.336 s). From observations of the Moon we measured the system noise contribution of 800 K. The dynamic range of raw data is about 30 dB, and the dynamic range of clean maps is $\sim$ 20 dB. The dynamic range is limited by the accuracy of phase measurements.

The absolute positional accuracy for SSRT images is generally not sufficient for accurate coalignment with other solar images in order to study features within active regions. The positional accuracy can be improved using standard methods.

3. Overview of observational data

The SSRT observes the Sun every day during about 02–08 UT in winter and during 00–10 UT in summer. SSRT images (one pair per day,

Stokes I and V) are available at the sites http://ssrt.iszf.irk.ru/ssrt, http://www.eastsib.ru/~ssrt/, http://www.ssrt.org.ru/. These sites also show high-time-resolution time profiles since June 2000. Calibrated SSRT data in the FITS format, also one pair per day, are accessible via anonymous ftp at ftp://iszf.irk.ru/pub/ssrt_data /fits/. Raw SSRT data files (special format) are stored at CD-R's along with some Stokes I and V maps per day in FITS files. The typical length of raw data files is 30–40 Mbytes for routine records (one hour record) and of order 100 Mbytes for high-time-reolution records. We have developed an application with the graphics user interface to process raw SSRT files, which performs all operations described above. In particular, this application produces files in FITS format, which can be viewed and analyzed using standard software.

3.1. Data overview

The first observation mode implemented on the SSRT was one-dimensional imaging using drift scans, where the Earth's rotation carried the Sun through the antenna beam (Smolkov *et al.*, 1986; Zubkova *et al.*, 1990; Nefedyev *et al.*, 1993). In this mode, a single spatial profile of the Sun with a resolution of up to $15''$ is formed in about two minutes. The sampling interval is about 0.3 s. The SSRT produces typically of order 150 drift scans per day at a single frequency, with the interval between them being of order 3 minutes. This is possible due to the multi-maximum beam of an equidistant linear interferometer: the position of each interference maximum on the sky is rigidly fixed, and the antennas follow the Sun during the daytime.

Then two-dimensional mapping from one-dimensional observations was implemented using Earth rotation aperture synthesis techniques (Alissandrakis *et al.* 1992). The resolution obtained in these maps was of order $15'' \times 45''$ (Sych, Uralov, and Korzhavin, 1993; Uralov *et al.*, 1998a). After the implementation of two-dimensional imaging in the correlation mode in 1996, we use the correlation-mode maps almost exclusively.

In the course of observations, the SSRT underwent several upgrades of the receiving system and low-noise amplifiers in the waveguide system. The major changes in the observational modes were:

- In 1992, the one-dimensional imaging by means of the frequency scanning put into operation to improve the temporal resolution up to 56 ms (Altyntsev *et al.* 1994).

– In 1993, the multi-frequency filter-bank receiver was equipped with a Fast Data Acquisition System (FDAS). This improved the time resolution to 14 ms (Altyntsev *et al.* 1996a).

– Two-dimensional imaging was performed since early 1996 with AOR (Uralov *et al.* 1998b) and from fall of 1996 till 2000 with MFB (Blinov *et al.* 1996). The imaging technique which we used with data from these two receiver systems was slightly different. Using MFB data, two solar images per day were produced, and the formation time for a single image was 20 to 60 minutes. Using AOR data, the imaging is performed during the whole daytime. In 1996–1999, we used an integration of several images during 20 to 60 minutes to enhance the sensitivity.

– After 2000, two-dimensional imaging is performed simultaneously with high-time-resolution one-dimensional imaging (14 ms) of the $EW + NS$ combination. Since the summer of 2000, we use AOR single-pass images only, and do not perform multi-channel recording from MFB.

All these are the reason for the several changes of the time resolution and sensitivity. Further details are given in Table 1. The table shows the time resolution of the SSRT in the one-dimensional mode and the sensitivity in the two-dimensional mode.

In addition to the imaging SSRT data, we have total flux data recorded with the radio polarimeter at 5.7 GHz located at the SSRT site. These light curves along with routine 0.3 s 1-D SSRT recordings provide information about events occurring during the observational daytime.

High-time-resolution data are only retained for events with subsecond-timescale fluctuations.

4. SSRT observations of the quiet Sun

4.1. General features

The SSRT is unique in that it can yield well-sampled maps of an area at least three solar diameters across, in three minutes or so. It can be used to make maps showing all spatial scales, from the solar disc itself down to the spatial resolution ($21''$ in the two-dimensional mode). The fluctuation sensitivity allows seeing low-contrast and large-scale features like filaments or coronal holes against the background of the solar disk and

Table I. SSRT data types available for different years

	1D			2D[1]		
	0.3 s	56 ms	14 ms	10 000 K	5 000 K	1 500 K
1983-1991	MFB					
1992	MFB	AOR: EW[2]				
1993	MFB	AOR: EW & NS	FDAS: EW			
1994	MFB	EW & NS	EW			
1995	MFB	EW & NS	EW			
1996	MFB & AOR		EW	AOR		MFB[3]
1997	MFB & AOR		EW	AOR	AOR	MFB
1998	MFB & AOR		EW		AOR	MFB
1999	MFB & AOR		EW		AOR	MFB
2000	MFB & AOR		AOR: EW+NS[5]			AOR[4]
2001	MFB & AOR		EW+NS			AOR
2002	MFB & AOR		EW+NS			AOR
2003	MFB & AOR		EW+NS			AOR

[1]Total sensitivity essentially determined by the solar noise contributions

[2]Linear interferometers are specified, the signals of which are recorded

[3]Two 2-d images per day. The formation time for a single image is 20–60 min in this mode only (MFB, 1997-2000)

[4]Single-pass images

[5]Combination of responses of two linear interferometers EW + NS

prominences against the sky. The dynamic range allows observing low-contrast features simultaneously with observations of bright sources in active regions.

Emission at the SSRT working frequency is characterized by a relatively large contribution of gyroresonance and thermal free-free emission with respect to higher frequencies, and by a moderate contribution

of thermal free-free emission with respect to lower frequencies. A high contrast of radio sources with respect to the quiet Sun is typical of the SSRT working frequency. The brightness temperature of steady radio sources in active regions can exceed 2 megakelvin (MK) at 5.7 GHz.

Below we illustrate these features with some SSRT data obtained for different phases of the solar activity cycle.

4.2. Comparison of an SSRT map with images observed in other spectral domains

Figure 7a shows an example of SSRT observations in total intensity. This is an averaged SSRT map observed close to the solar minimum, on 6 October 1997. This example of observations of a relatively quiet Sun is interesting also in connection with the approaching solar minimum. The moderate brightness of the observed radio sources permits using dirty SSRT maps. For comparison, Figure 7 also shows Hα data from Big Bear Solar Observatory (b) and radio data at 17 GHz from NoRH (c), SOHO/EIT images at 304 Å (d) and 171 Å (e) as well as the Yohkoh/SXT image (f).

All images are centered, evenly oriented (solar North is up), resized to the same spatial scale, and nonlinearly displayed to show both bright sources and the quiet Sun. We removed the limb darkening from the Hα image and 're-rotated' it from 5 October, 15:43:59 UT to 6 October, 02:25:57 UT to compensate for the solar rotation and to make the comparison easier. We averaged three SSRT maps, eight NoRH 1s-snapshots produced with an interval of 10 min as well as 19 Yohkoh/SXT images to suppress the fragmentation of low-contrast features in NoRH snapshots and to enhance the sensitivity. All these images before the averaging are also 're-rotated' to the same time. The SOHO/EIT images are degridded and flat-fielded. The three SSRT maps used in the averaging are formed in 48, 33, and 10 minutes.

The SSRT map at 5.7 GHz shows a wider range of brightness compared with the NoRH map at 17 GHz. This is because of the greater contribution of coronal emissions at lower frequencies. In particular, the maximum brightness temperature in the SSRT map is 75 700 K (source 1), while in the NoRH map this source has $T_B = 18\,000$ K. These brightness temperatures suggest that we are dealing with optically thin radio emission. In general, for optically thin thermal bremsstrahlung of a source with a kinetic temperature of $T \gg T_{QS}$ we expect the ratio $(T_{B\,5.7} - T_{QS\,5.7})/(T_{B\,17} - T_{QS\,17})$ to be equal to $(17/5.73)^2 = 8.8$. Note that the quiet Sun's level in the NoRH image analyzed is 10 370 K. This ratio is 7.8 for source 1 and 6.7 for source 2. The disaccord of the measured values with the expected ratio can be due to 1) different

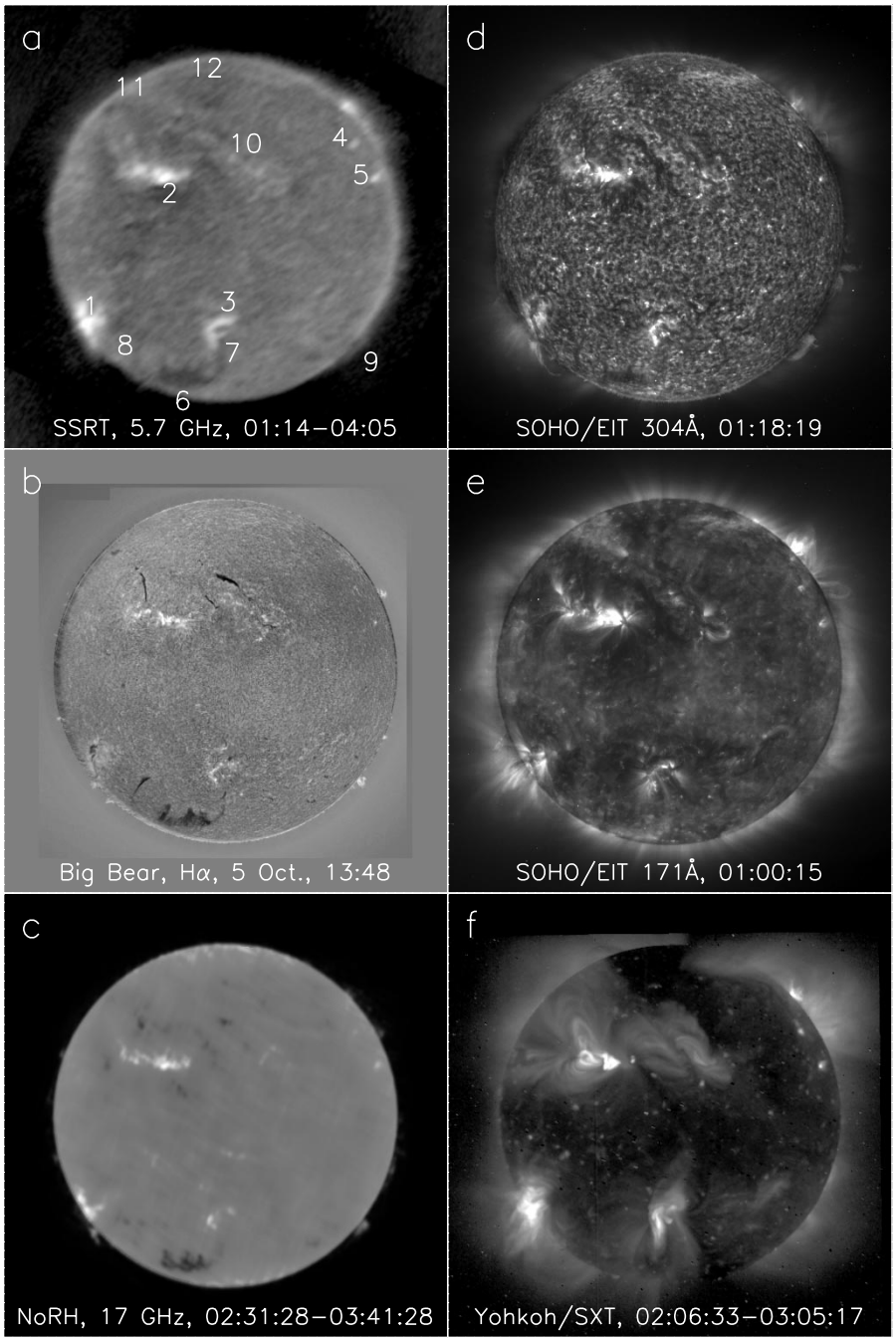

Figure 7. Comparison of an SSRT Stokes I dirty map of 6 October 1997 with data from other spectral domains. All images are nonlinearly processed to make both bright sources and the quiet Sun pronounced. Solar North is up.

spatial resolution for both instruments (the cross section of the beam is typically 25″ for the SSRT and 15″ for NoRH), which results in different contamination of the bright features with darker environment, 2) limited of the sensitivity of the NoRH, 3) artifacts of the CLEAN routine in NoRH images when the brightness of a source is close to the CLEAN level of 3 000 K (Maksimov *et al.* 2001), and 4) imaging and calibration errors in both images. Taking into account all these factors, we conclude that these values do not contradict optically thin free-free thermal emission.

Generally, the bright coronal features in SSRT maps are mostly similar to the SOHO/EIT 171 Å and 195 Å images (T_{peak} = 1.3 MK and 1.6 MK). However, the 'F'-shaped feature (3) in the SSRT map has the best similarity with higher-temperature images observed by SOHO/EIT at 284 Å (T_{peak} = 2.0 MK, not shown) and soft X-rays ($T > 2$ MK). Plages and/or dense emitting plasmas above them in the corona are visible in the SSRT map. One of them is a bright region extended across bright source 2. Its brightness temperature is $(32 - 54)\,10^3$ K. A bright region around source 1 represents a coronal counterpart of a plage with $T_B = (33 - 58)\,10^3$ K. Note that there is also a dark filament in this region, which complicates the situation. Extended bright region 10 is one more plage field.

Coronal ('X-ray') bright points are detectable in all images, and even in Hα. However, feature 4 ($T_{B\,5.7}$ = 31 000 K) is not well pronounced at 17 GHz ($T_{B\,17}$ = 11 900 K). The brightness temperature for feature 5 is 43 000 K at 5.7 GHz and 14 000 K at 17 GHz. Still more bright points can be found by careful comparison of the SSRT and soft X-ray images. Their brightness temperatures in SSRT images are typically some 10^4 K, and they also show a general agreement with optically thin free-free emission (Maksimov *et al.* 2001). In this case, the ratios of the brightness temperatures calculated for the optically thin limit are 8 for feature 5 and 10.5 for feature 4.

Dark region 12 close to the North Pole matches the darkest part of a coronal hole well visible in SOHO/EIT 171 Å and Yohkoh/SXT images. Coronal holes that are often visible in SSRT images are generally inhomogeneous, with brighter and darker portions (Krissinel *et al.* 2000). This fragmentation makes coronal holes at 5.7 GHz not as pronounced as in soft X-ray images. Therefore, contours of coronal holes observed at 5.7 GHz are located inside coronal holes visible in extreme ultraviolet and soft X-rays, and they are fragmented. In particular, coronal hole 12 has an average brightness temperature $\overline{T}_{B\,5.7}$ = 12 490 K for the whole region visible as a dark feature at 5.7 GHz, and the deepest depression has $\overline{T}_{B\,5.7}$ = 10 900 K. It is not detectable at 17 GHz. Generally, coronal holes at 17 GHz are sometimes manifest as fragmented features, but

they are not distinct (Gopalswamy *et al.* 1998, Krissinel *et al.* 2000). To a first approximation, the more pronounced coronal contribution at 5.7 GHz (38% on the average, considering T_{QS}) is an apparent explanation of these facts.

Dark filaments and filament channels are also visible at 5.7 GHz. Filaments must be optically thick at both 5.7 and 17 GHz, but at 5.7 GHz they are observed with higher contrast and show more details. For example, the configuration of dark filament 6 is more conspicuous at 5.7 GHz, where it shows extended northward features 7 ($\overline{T}_{B\,5.7} = 13\,560$ K, $\overline{T}_{B\,17} = 9\,830$ K), and 8 ($\overline{T}_{B\,5.7} = 14\,850$ K, $\overline{T}_{B\,17} = 10\,420$ K). Feature 8 is still more pronounced in later images which are not shown. In this example, the brightness temperature of the darkest part of the filament is 5 000–8 400 K, with an average of 6 800 K at 17 GHz (the contrast of 1.5:1), while the corresponding values are 6 100–12 500 K and 8 500 at 5.7 GHz (the contrast of 1.9:1). At about 13 UT that day, that filament was ejected.

Another dark filament is seen in the northeast part of the disk, with well-pronounced darkest portion 11 close to the limb ($\overline{T}_B = 13\,800$ K at 5.7 GHz, and at 17 GHz it is not detectable, $\overline{T}_B = 10\,600$ K). The brightness temperature of the filament is not as low, 12 500–14 000 K, probably, because the filament is not well resolved. Also, dark filaments and filament channels with $T_B = (9 - 12)\,10^3$ K fringe region 10 from the southeast and northwest.

The dark feature just under the label 2 apparently has counterparts in the SOHO/EIT 304 Å and NoRH images. However, it can also be due to a side lobe from bright source 2.

Some filaments not detectable with NoRH are nevertheless visible in SSRT maps (Zandanov and Lesovoi 1999). An apparent explanation of all these facts is the higher contrast with the quiet Sun ($T_{QS} = 16\,000$ K at 5.7 GHz and $T_{QS} = 10\,000$ K at 17 GHz). The higher brightness temperature of filaments in SSRT images with respect to NoRH images is due to somewhat worse spatial resolution of the SSRT which increases contamination of the filaments with brighter environment, and, probably, due to different contribution of the corona-prominence transition region at 5.7 and 17 GHz (Drago 1990). Filaments with higher kinetic temperature, about 10 000 K, are obviously not visible at 17 GHz, but still visible at 5.7 GHz.

Extended feature 9 above the southwestern limb is a prominence identifiable in SOHO/EIT 304 Å and NoRH images. Its shape does not resemble well the prominence in Hα image apparently because this picture was obtained about 12 hours before, and the 're-rotation' we used is not three-dimensional. The average brightness temperature of the prominence as seen at 5.7 GHz is 10 600 K, and it is 3 400 K at

17 GHz (the same region). The average brightness temperature of the prominence portion visible at 17 GHz is 13 000 K at 5.7 GHz and 8 500 K at 17 GHz.

The discussed items of radio observations at 5.7 and 17 GHz provide, in particular, an identification criterion if a dark feature observed in radio images can be either a filament or a coronal hole: if this feature is dark both at 5.7 and 17 GHz, it is a filament or a filament channel, not a coronal hole. This criterion can be useful if no other data are available.

4.3. Polarization data

Measurements of the coronal magnetic fields from radio data have been extensively addressed (e.g., Kundu 1965; Kundu and Alissandrakis 1984; Gelfreikh, Pilyeva, and Ryabov 1997; Alissandrakis *et al.* 1996). Polarization data produced with the SSRT were analyzed by Maksimov and Bakunina (1991, 1995) and Uralov *et al.* (1998b). Hence, we briefly mention here only a few points relevant to this issue.

In the simplest case, when we observe free-free emission from a homogeneous, thermal, optically thin, hot plasma within large-scale, weak coronal magnetic field $B < 200$ G, we expect the emission to be circularly polarized in the sense of the x-mode with a degree $r_c \approx 2\cos\theta(\nu_B/\nu) \approx 10^{-3}B\cos\theta$ at 5.7 GHz, where θ is the viewing angle relative to the direction of the magnetic field (Zheleznyakov 1970, Dulk 1985). The same factor $\cos\theta$ applies to the degree of polarization of radio emission and to the longitudinal magnetogram.

However, the magnetic fields diverge and hence fall off with height in the corona, thus decreasing in strength and increasing in spatial extent. In addition, the obvious effect is the averaging of the observed quantities within the beam of the instrument, and it is more important for compact features. Thus, comparisons of the degree of polarization with the photospheric magnetic fields can disagree with the estimate given above. Gyroresonance effects at harmonics of the gyrofrequency in stronger magnetic fields can still more complicate the situation, and it is not possible to judge about magnetic fields in those cases without radio spectra.

Figure 8 shows a photospheric magnetogram and SSRT polarization data for the same observation of 6 October 1997 shown in Figure 7. The left panel (a) shows a SOHO/MDI magnetogram for that day, at 01:39:03 UT (black corresponds to S-polarity, and white corresponds to N-polarity). The right panel (b) shows the same SSRT map in total intensity as in Figure 7a, and it is overlaid with black $\pm 5\%$ contours of the polarization.

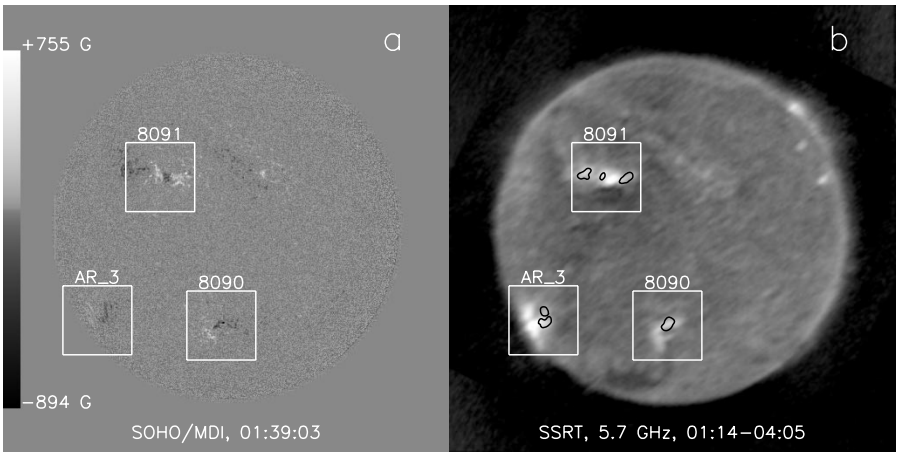

Figure 8. Comparison of the SSRT polarization map of 6 October 1997 with a photospheric magnetogram. a) SOHO/MDI magnetogram of October 6 1997, 01:39:03 UT. b) SSRT Stokes I map (halftone, same as in Fig. 7a) overlaid with contours of the degree of polarization computed from the SSRT Stokes I and V maps under the assumption of optically thin emission. Contour levels are $\pm 5\%$. Halftone images are nonlinearly displayed to show both bright and faint features. Solar North is up.

The overall picture of the magnetic fields at the photosphere is rather simple. There are three active regions on the solar disk with rather weak magnetic fields, AR 8090, AR 8091, and one more, weak region at southeast with no name, which we labeled AR_3. Enlarged images of these regions marked in Fig. 8a by white boxes along with contours of the radio polarization are shown in Figure 9, left panels a, c, and e.

Black contours on the enlarged images show a positive degree of circular polarization of the radio emission, and white contours show a negative polarization (reversed with respect to the magnetogram for clarity). Contour levels are $\pm 5\%$ and $\pm 15\%$. Three panels b, d, and f show three enlarged regions of the SSRT Stokes I image from Fig. 8b. In the computation of the degree of polarization, all pixels, corresponding to pixels in Stokes I and V maps with values below the sensitivity level or below the dynamic range with respect to the brightest source, are zeroed everywhere in the map. This technique can miss weaker polarized sources, and careful analysis is required to detect them. The degree of polarization is computed under the assumption of optically thin emission, i.e., the quiet solar disk of 16 000 K is subtracted from the Stokes I map.

The configuration shown by the degree of polarization resembles the photospheric magnetogram. The sense of polarization of radio emission corresponds to the x-mode.

Relatively strong magnetic fields are concentrated in compact or thin features. The maximum photospheric magnetic fields are -894 G (AR 8090) and $+756$ G (AR 8091). The maximum brightness temperature in the SSRT Stokes V map are $-5\,700$ K and $+4\,800$ K.

To ascertain that the radio data do not contain any contribution of the gyroresonance emission, we compare the total intensity of the microwave emission with soft X-ray emission. Soft X-ray emission is due to emission lines and thermal bremsstrahlung of optically thin hot plasmas ($T > 2$ MK). The brightness of the soft X-ray emission is proportional to the column emission measure. The brightness of the thermal free-free radio emission is proportional to the column emission measure and has a weaker dependence on temperature $T^{-1/2}$. Therefore, if we compare the optically thin thermal free-free emission in microwaves with soft X-ray images, we expect them to resemble each other. However, if gyromagnetic radio emission is present, it would show up as compact bright radio sources in regions where the circular polarization is conspicuous without counterparts in soft X-rays.

Figure 10 shows normalized one-dimensional vertical spatial profiles computed from the SSRT total intensity map (quiet solar disk subtracted) and from the soft X-ray image observed with Yohkoh/SXT (shown in Fig. 7f). This one-dimensional representation is more convenient for the comparison and shows some quantitative features. We also plot in Figure 10 the spatial profile of the circular polarization (Stokes V, gray-dashed). To suppress the instrumental effects and noises, the SSRT Stokes V map is processed in the same manner as the degree of polarization described above. To simulate the instrumental smoothing, we convolved the soft X-ray image with the model of the SSRT beam. The spatial profile of the polarization is shifted upward by 0.5 to show it better.

Figure 10 shows that both microwave intensity and soft X-ray one-dimensional profiles mainly resemble each other well. The trough in the middle part of the soft X-ray profile is due to the large-scale depression in the soft X-ray image to the south from the equator. However, this area is not dark in microwaves due to the presence of plasmas with $T < 2$ MK visible in SOHO/EIT 171 Å image. There are many other features detectable in these profiles. For instance, a compact depression in the microwave profile around $-860''$ is due to dark filament 6 (see Fig. 7). The depression in soft X-rays from $700''$ northward is due to the north polar coronal hole, which is not so clearly pronounced at 5.7 GHz.

We see no gyromagnetic peaks in the microwave intensity spatial profile, and all peaks in it match peaks in the soft X-ray profile. In particular, we note that the microwave intensity in polarized regions

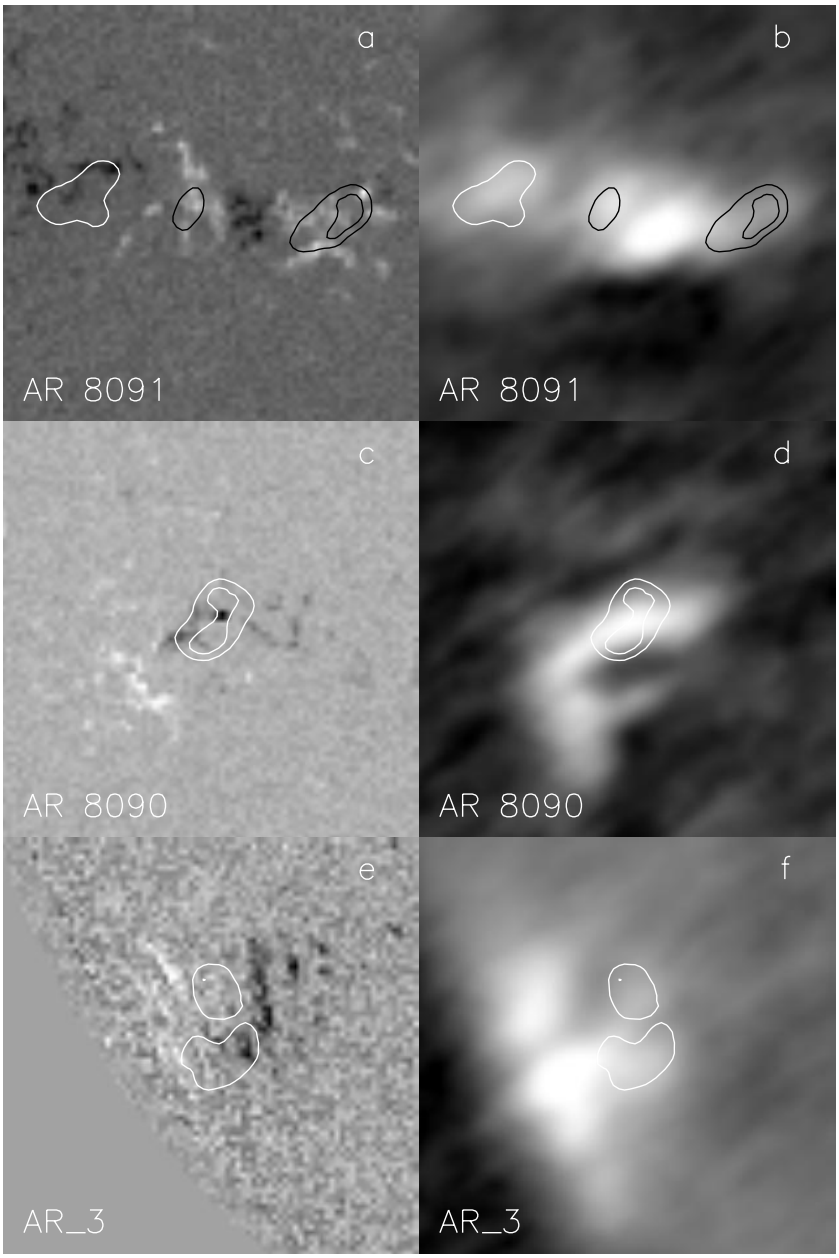

Figure 9. Comparison of the SSRT polarization map of 6 October 1997 with a photospheric magnetogram. (a,c,e) Enlarged parts of the magnetogram marked in Fig. 8a by white frames overlaid with contours of the degree of polarization. (b,d,f) Corresponding enlarged parts of the Stokes I map overlaid with the same contours (Fig. 8b). Contour levels are $\pm 5\%$ and $\pm 15\%$ (black positive, white negative). Halftone images are nonlinearly displayed to show both bright and faint features.

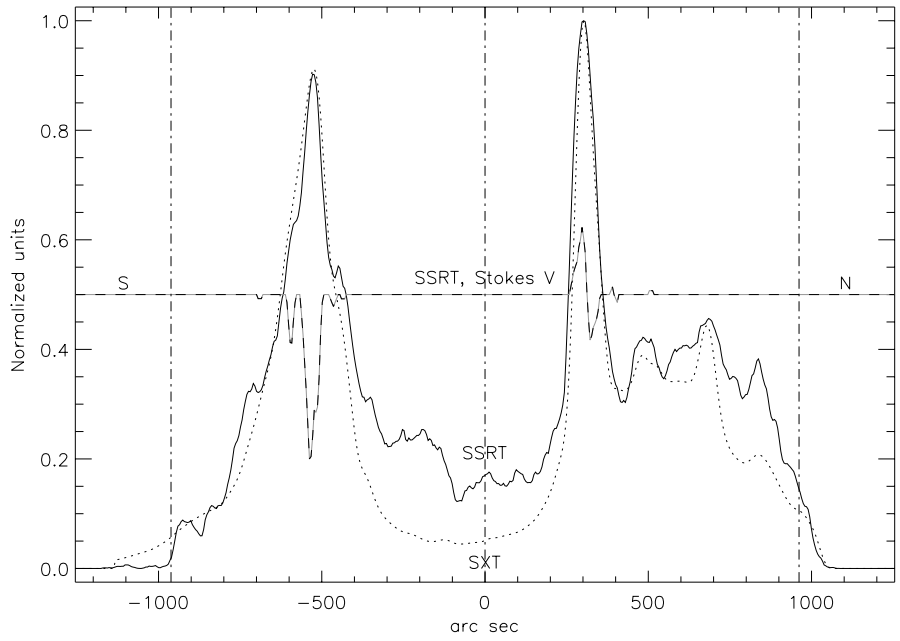

Figure 10. Comparison of one-dimensional microwave and soft X-ray spatial profiles in S–N directions. Solid: SSRT, Stokes I. Dotted: soft X-rays. Gray dashed: SSRT, Stokes V shifted by 0.5 upwards. The quiet solar disk is subtracted from the SSRT Stokes I map. Yohkoh/SXT image is convolved with a model of the SSRT beam. The horizontal axis shows arc seconds from the solar disk center. Vertical dash-dotted lines show the solar disk center and the photospheric radius.

coincides closely with soft X-rays. All this suggests that the estimate of the degree of circular polarization for free-free thermal emission applies to the data under consideration.

Figure 11 illustrates the measurements of the magnetic fields averaged over polarized areas visible in the Stokes V map and the corresponding regions in the magnetogram. Triangles connected with the solid curve show the coronal magnetic fields inferred from the SSRT data. Squares connected with the dotted curve show the values measured from the magnetogram. Six points show six polarized regions. The figure shows that the measurements from radio data and from the photospheric magnetogram are rather close. There exist, however, many obvious reasons for differences. More detailed analysis of these data is beyond the scope of this paper.

Another possibility for measurements of coronal magnetic fields at larger heights from SSRT data is to use polarization reversal effects in the propagation of the microwave emission through regions of quasi-transverse magnetic fields (Ryabov and Maksimov 1999).

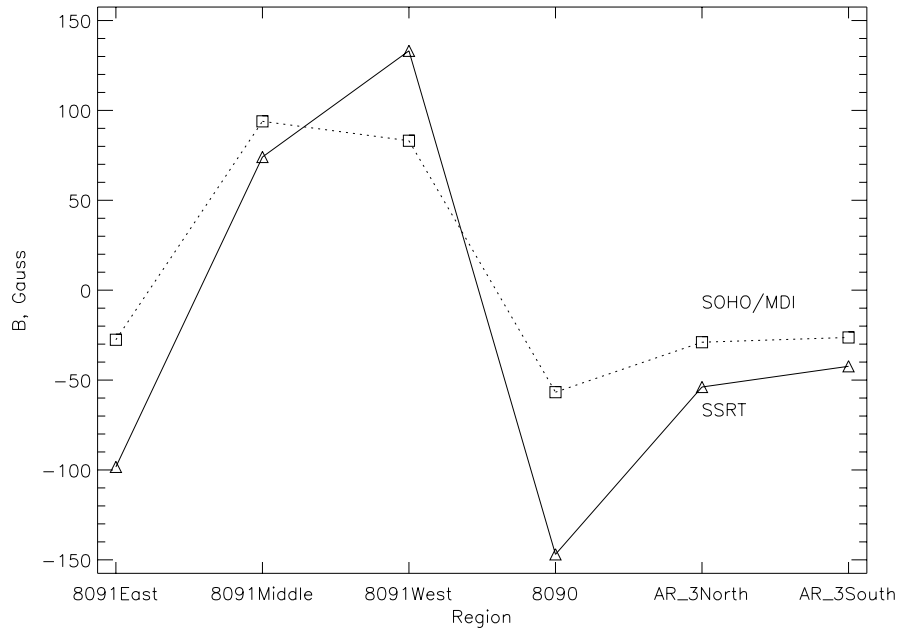

Figure 11. Comparison of the estimates of the coronal magnetic field inferred from the polarization measurements at the SSRT with the photospheric magnetogram produced by SOHO/MDI. Plotted values are averaged within the polarized areas in the Stokes V map and the corresponding regions in the magnetogram. Triangles connected with the solid curve show estimates obtained from the microwave data. Squares connected with the dotted curve show measurements from the magnetogram.

5. Observations of dynamic phenomena

5.1. Eruptive prominences and a post-eruptive flare

The SSRT observes eruptive filaments and prominences (Lubyshev *et al.* 1996, Maksimov and Nefedyev 1991, 1992, Uralov *et al.* 2002). An example is shown in Figure 12. The figure shows a CME-associated loop-like eruptive prominence ejected on 14 January 2001 from a northwest polar region. The eruption is recorded in about fifty frames with an average interval of order 2.5 minutes, and six of them are shown in the figure. The brightness temperature of the prominence is typically less than 15 000 K. To make it more visible, the brightness of images is limited at 15 000 K, which causes apparent 'blurring' of the solar disk. There is a hump on the solar limb at the western end of the loop-like prominence, and this distorts the circular shape of the disk. Fragments of the prominence in the figure can be detected up to two solar radii from the solar disk center.

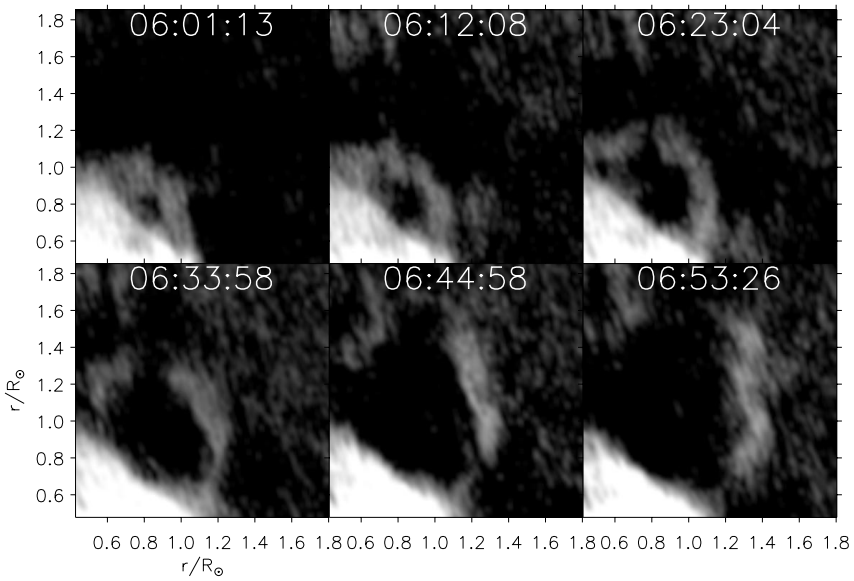

Figure 12. An eruptive prominence observed on 14 January 2001. The brightness of images is limited at 15 000 K to make the prominence pronounced, and this results in blurring the solar disk. Axes show distances from the solar disk center in fractions of the solar radii.

Another example is presented in Figure 13. It shows four frames of a record of an eruptive prominence observed with the SSRT on 4 September 2000. The event started with an activation of the filament on the solar disk, where there was no active region. The SSRT recorded the motion of the filament across the solar disk and its subsequent motion on the background of the sky. The images in Figure 13 show the ejecta also during the latter stage, when its twin-loop-like configuration is well visible.

The eruption of 4 September 2000 was followed by a weak large-scale two-ribbon flare associated with the formation of a post-eruptive arcade. The flare occurred in the region where the initial filament was located, beyond any active region. The absence of strong magnetic fields determined, in fact, an entirely thermal character of the post-eruptive flare. For this reason, the images of the flare in Hα, microwaves, and soft X-rays match each other well (Figure 14). The figure shows as a halftone: a composite soft X-ray image produced from several Yohkoh/SXT frames in the interval of 06:06–06:16 UT to enhance the sensitivity and dynamic range (a), an SSRT image composed of five frames in the interval of 06:04–06:17 UT to fit the interval of the composite soft X-ray image (b), an Hα image obtained at 06:32:25 UT at Kanzelhoehe Observatory (c), and an SSRT image obtained at the

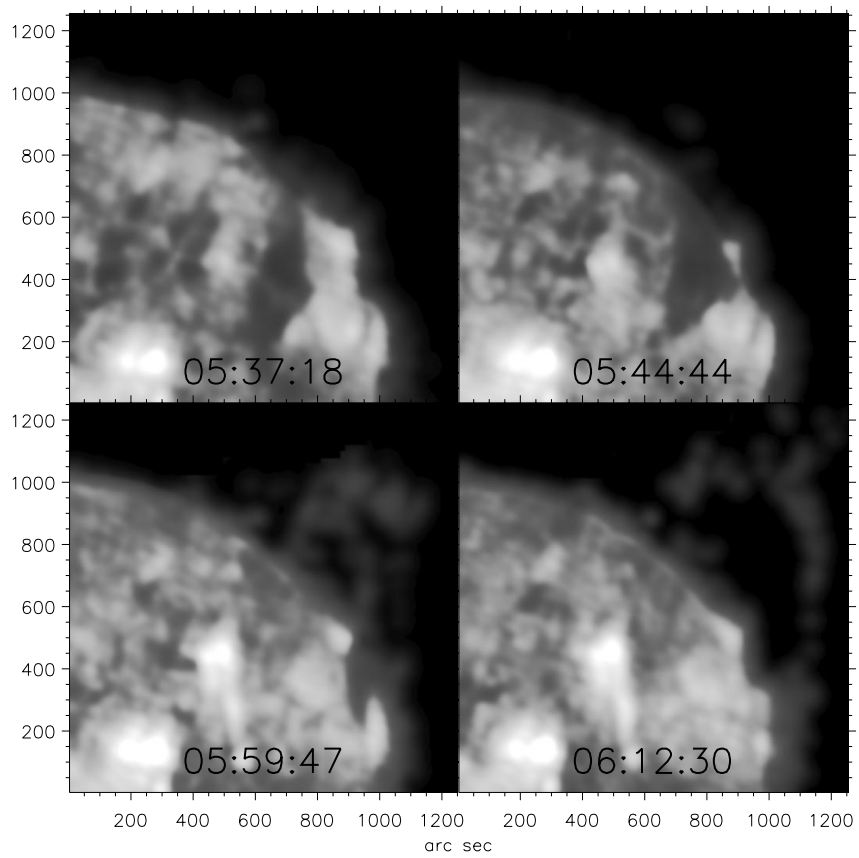

Figure 13. An eruptive prominence observed with the SSRT on 4 September 2000 (four frames of forty). Axes show arc seconds from the solar disk center.

same time as Hα image (d). Contours overlaid on the soft X-ray and Hα images show the SSRT images. Contour levels are $[24, 48, 96] \times 10^3$ K. A good correspondence is seen of the microwave and soft X-ray images. Bright features in Hα, i.e. footpoint regions of loops constituting the post-eruptive arcade, also correspond to its image visible in soft X-rays and microwaves.

The thermal character of the flare is also illustrated with light curves shown in Figure 15. Three light curves are shown in this figure: total flux time profiles computed for the flare region from SSRT data (solid), NoRH data (dashed), and the thermal radio flux predicted by GOES soft X-ray data (dotted). The total radio flux is computed as

$$S_{[sfu]} \approx 7.22 \times 10^{-11} \nu^2_{[GHz]}\, \rho^2_{[arcsec]} \sum_i T_{Bi[K]},$$

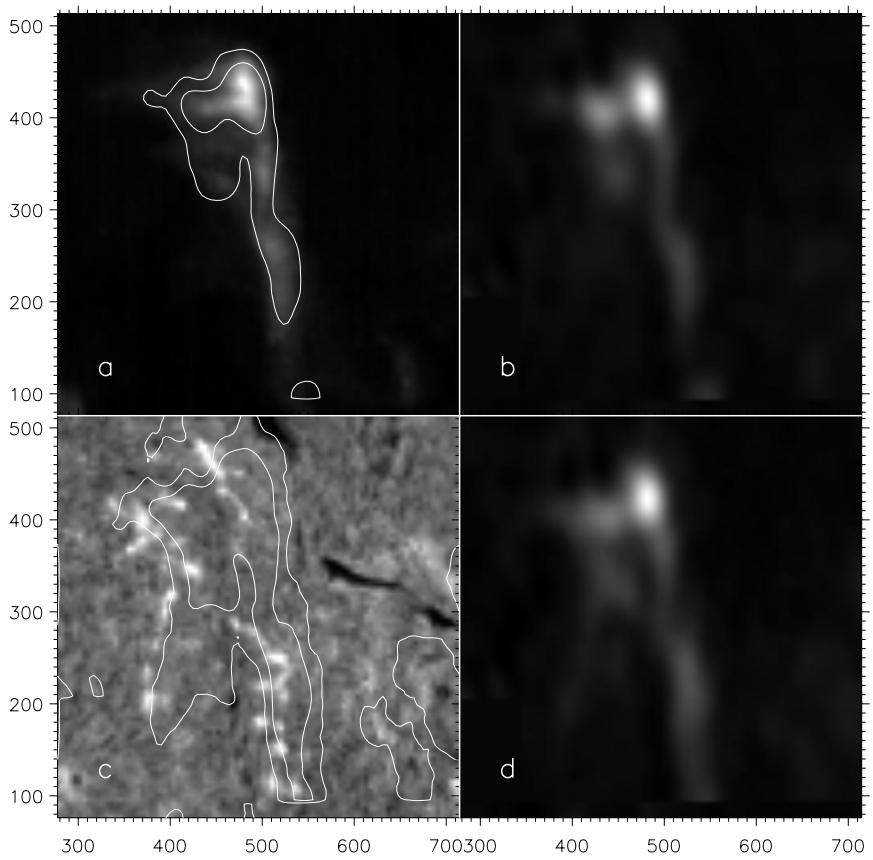

Figure 14. Images of a post-eruptive thermal flare of 4 September 2000. a) soft X-rays (Yohkoh/SXT), composite image of 06:06–06:16 UT overlaid with contours of the SSRT image (b). Contour levels are 48 000 and 96 000 K. b) SSRT, 5.7 GHz, 06:04–06:17 UT; c) Hα, Kanzelhoehe Observatory, 06:32:25 UT overlaid with contours of the SSRT image (d). Contour levels are 30 000 and 60 000 K. d) SSRT image of 06:31–06:33 UT. Axes show arc seconds from the solar disk center.

where T_{Bi} is the brightness temperature of a pixel (with a width ρ).

The thermal radio flux is computed from soft X-ray data as

$$S_{[sfu]} \approx 3 \times 10^{-45} EM_{[cm^{-3}]} T_{[K]}^{-1/2}$$

(Grechnev 2003). The emission measure EM and temperature T of the emitting plasma are computed from GOES data using the GOES software by R. Schwartz. The light curves computed from SSRT and GOES data are smoothed over five points to suppress jumps due to the insufficient accuracy of the calibration and computations. The level of the quiet Sun is subtracted from SSRT and NoRH data. The presence of

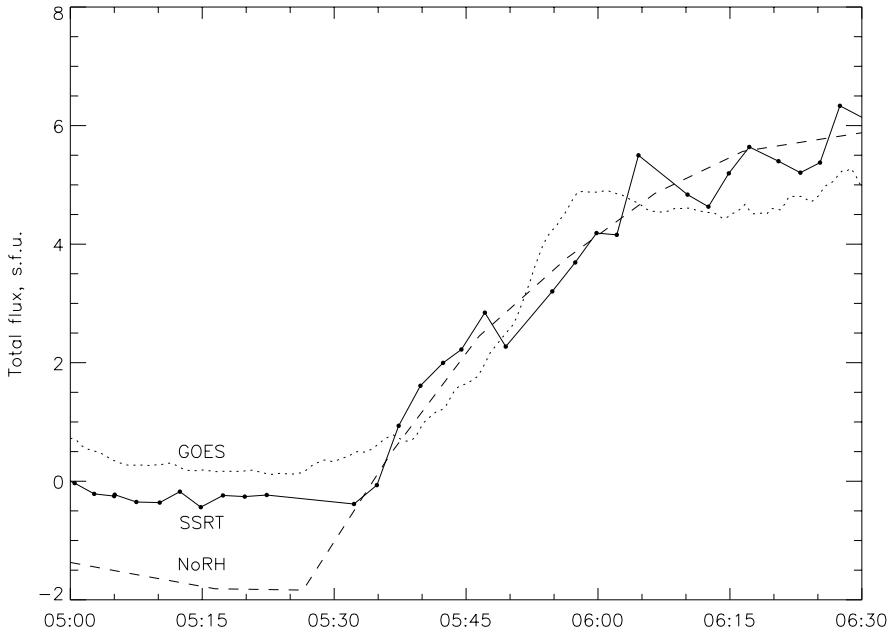

Figure 15. Total flux time profiles of the post-eruptive flare observed on 4 September 2000: SSRT at 5.7 GHz (solid), NoRH at 17 GHz (dashed), thermal radio flux predicted by GOES soft X-ray data (dotted). Samples at 5.7 GHz are marked with filled circles. GOES and SSRT light curves are smoothed over five points.

a dark filament in the event region before the flare determines negative values of the pre-flare total flux.

All three light curves are close, which supports the thermal nature of the flare. They also illustrate the average accuracy of the calibration of the SSRT data. It seems satisfactory. However, the frame-to-frame stability of the calibration is worse, at best 30%, especially when SSRT maps contain much brighter sources.

This eruptive event including the weak post-eruptive flare was analyzed by Uralov *et al.* (2002). Flares that are more powerful were analyzed by Altyntsev *et al.* (1998, 1999) using one-dimensional SSRT data, and by Altyntsev *et al.* (2002) using two-dimensional SSRT data.

5.2. High-time-resolution one-dimensional observations

To study the phenomena of the shortest timescale, we use the one-dimensional mode. Up to now, the SSRT has supplied spatially resolved solar radio data of the highest temporal resolution. High-time-resolution observations with a one-dimensional resolution of up to 15″ are performed simultaneously with two-dimensional mapping. These data are retained for events with fine time structures. The time resolution of

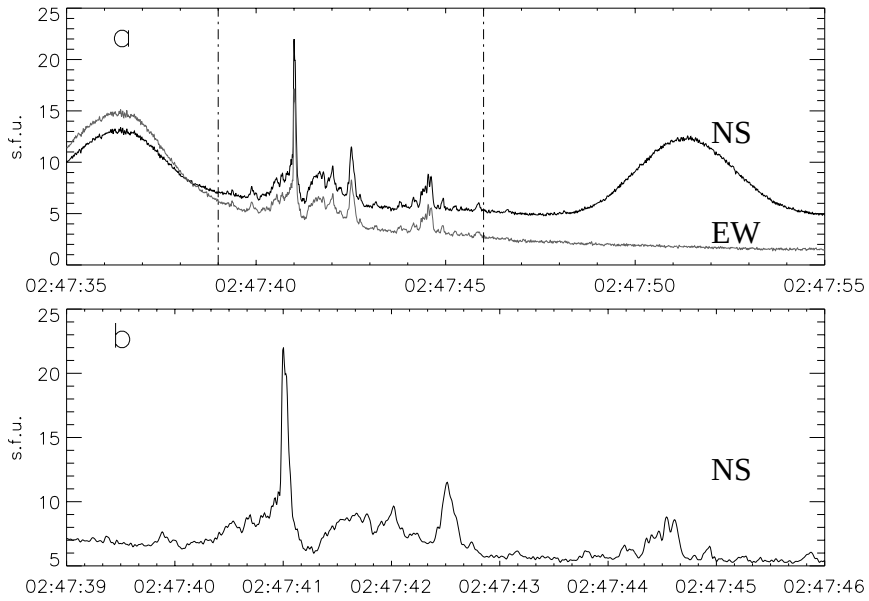

Figure 16. High-time-resolution one-dimensional record (Stokes I) produced from the raw record of 13 August 2002. a, part of the time profile within the interval marked in Fig. 5 by vertical dash-dotted lines; b, expanded time profile within the interval marked by vertical lines in the upper panel (a). The time resolution is 14 ms.

these recordings is 14 ms. Total flux time profiles for separate compact sources composed of one-dimensional recordings with this time resolution have a sensitivity of 0.05 sfu.

An example of a high-time-resolution one-dimensional recording for the total intensity produced from the raw recording of 13 August 2002 (Fig. 5) is shown in Figure 16. The time profile within the interval marked in Fig. 5 by vertical dash-dotted lines is shown in the upper panel, and the expanded time profile within the interval marked by dash-dotted lines in the upper panel is shown in the lower panel.

To form the time profiles, an 'alignment' was carried out of the raw recordings of the impulsive sources along the directions corresponding to the responses of the EW and NS interferometers separately (shown in Fig. 5 by the arrows). Small 'strips' of $41''$ only are integrated covering the impulsive sources to exclude the contribution of the other sources on the solar disk. The difference of the smoother background in the time profiles formed for the EW and NS interferometers is due to the differing observing conditions for these interferometers. However, the impulsive components resemble each other well. There is no significant polarization in this event, and we do not show it.

Because the sum $EW + NS$ is used to form high-time-resolution data, the time profiles computed from one-dimensional data are contaminated by the response of the other interferometer (Fig. 16, outside of dash-dotted lines). This is negligible when rapid fluctuations under study are observed within time intervals, which are short relative to the pass time across radio sources.

Another example (Figure 17) shows a total flux time profile of an impulsive microwave source along with a dynamic spectrum obtained at the National Astronomical Observatory of China, NAOC (time resolution 5 ms) measured during the flare of September 17, 2001 (Altyntsev *et al.* 2003). The total flux time profiles are computed from SSRT high-time-resolution one-dimensional data by integrating the one-dimensional data over the region of the impulsive source. The time profiles obtained with both remote instruments at the same frequencies of 5.69 and 5.77 GHz show a reasonable accord. They also show that features in subsecond-timescale time profiles can be due to spectral features. We also see that this short burst is significantly polarized.

Using SSRT data, it is possible to estimate the drift rate and density gradient in regions where fast-drifting bursts are generated.

The spatial position of the impulsive source can be found as an intersection point of the projections of the knife-edge beams of the linear interferometers EW and NS onto the solar disk.

As for polarization data in the high-time-resolution one-dimensional mode, one has to be aware of an artifactitious polarization proportional to the derivative of the total intensity due to the time-sharing in the polarization measurements (Altyntsev *et al.* 1996a).

High-time-resolution one-dimensional SSRT data were used in studies of fine time structures in solar radio emission (e.g., Altyntsev *et al.* 1994, 2000). In particular, despite the seemingly poor angular resolution of the SSRT, a statistical analysis of those observations revealed a positional dependence of the source size on the solar disk in support of the scattering of centimetric radio emission in the solar corona (Altyntsev *et al.* 1996b).

6. Summary and concluding remarks

We have presented the current state of the SSRT and its observational modes after several upgrades carried out since 1992. Some of recent findings made from the SSRT data are outlined, and the observational capabilities of the SSRT are considered. Observational data acquired since 1983 are overviewed. Some data processing and analysis techniques are also addressed.

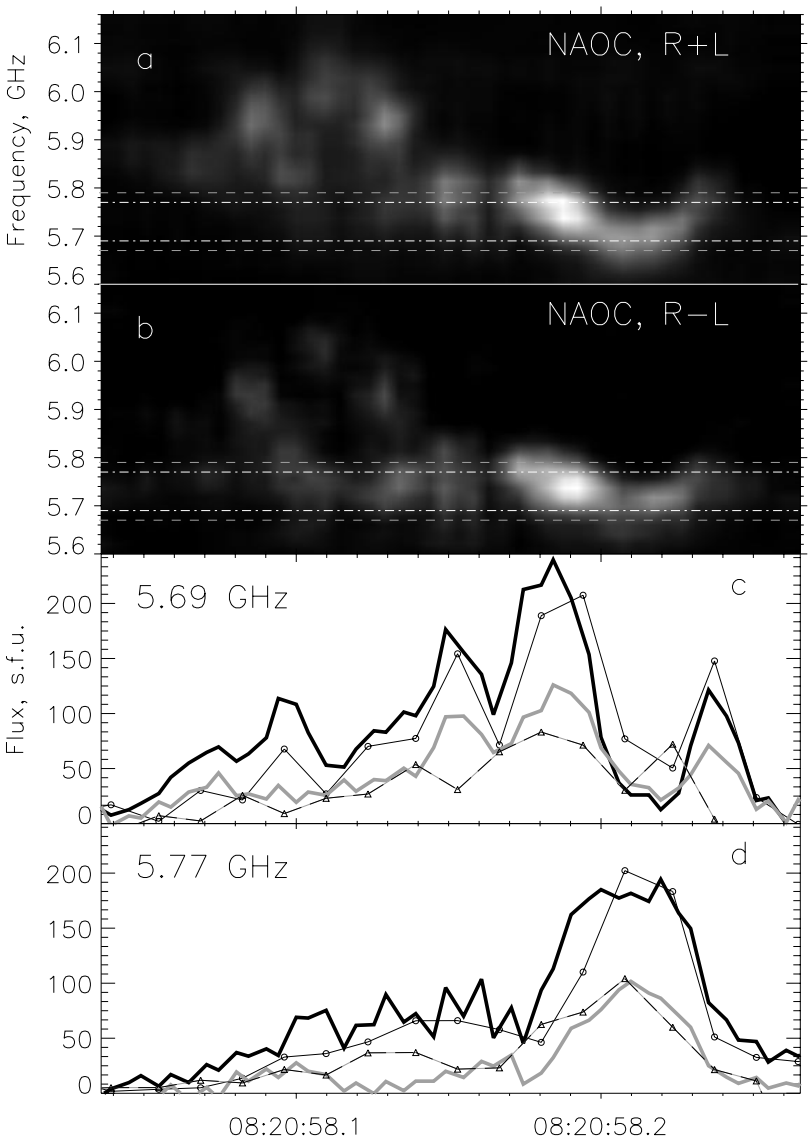

Figure 17. Dynamic spectrum and time profiles of a subsecond-timescale impulsive burst of September 17, 2001 flare. Panels (a) and (b) show the dynamic spectrum recorded at NAOC in the total intensity ($RCP + LCP$) and circular polarization ($RCP - LCP$) in the frequency range 5.2–6.4 GHz. White horizontal dash-dotted lines mark the frequencies of 5.69 and 5.77 GHz at which the burst was recorded at the SSRT (two interference orders, EW linear interferometer). Dashed gray horizontal lines mark the limits of the operating band of the SSRT. Panels (c) and (d) show single-frequency time profiles recorded with the NAOC spectropolarimeter (thick lines, black RCP, gray LCP) and total flux time profiles computed from the high-time-resolution SSRT record (solid RCP, dashed-gray LCP). Symbols mark sampling times of the SSRT record.

The observational capabilities of the SSRT are determined by the observing frequency of 5.7 GHz and instrumental characteristics. The spatial sensitivity allows good seeing all spatial structures from the spatial resolution (21″ in the two-dimensional mode) up to the field of view covering the entire solar disk and reaching three solar diameters. The sensitivity of the SSRT allows good seeing low-contrast and large-scale features like filaments or coronal holes against the background of the solar disk and prominences against the sky. The dynamic range allows observing the low-contrast features simultaneously with observations of bright sources in active regions.

The working frequency determines a relatively large contribution of gyroresonance and thermal free-free emission in SSRT data with respect to higher frequencies, and moderate contribution of the free-free emission with respect to lower frequencies. Polarization data from the SSRT allow measuring coronal magnetic fields. The high contrast of radio sources with respect to the quiet Sun is typical of the SSRT working frequency of 5.7 GHz. The brightness temperature of steady radio sources in active regions can exceed 2 MK at 5.7 GHz.

The SSRT observes dynamic phenomena such as eruptive prominences and solar flares. The rate of two-dimensional mapping is not sufficient for detailed imaging of short impulsive flares; however, high-time-resolution observations with a one-dimensional resolution of up to 15″ are performed simultaneously with two-dimensional mapping. The time resolution of these records is 14 ms. These data are retained for events with fine time structures. Total flux time profiles for separate compact sources composed of one-dimensional records with this time resolution have a sensitivity of 0.05 sfu.

We think about a further modification of the SSRT through the extension to the multi-frequency capability and change the operational principle to the parallel aperture synthesis (Zandanov, Altyntsev, and Lesovoi 1999, Lesovoi 2001). All these would extend the observational opportunities of the instrument.

Acknowledgements

We are grateful to T.A. Treskov, one of the principal designers of the SSRT, who passed away in 2000. We thank our colleagues from the Radio Astrophysical Department and the Radio Astrophysical Observatory in Badary. St. Petersburg Technical University, the Institute for Automatics and Electrometry and the Technological Design Institute of Scientific Instrument Engineering in Novosibirsk, the Institute of Applied Physics of Bern University contributed to the current state of

the SSRT. Operation of the SSRT is supported by the Russian Ministry for Industry, Technology and Science, Russian Foundation for Basic Research (RFBR), and Siberian Branch of Russian Academy of Sciences. We appreciate the experience, assistance and fruitful discussions with colleagues from the Nobeyama Radioheliograph.

We are also thankful to the INTAS, INTAS-RFBR, SCOSTEP, ISF, and ESO C&EE Programme for the support of the SSRT operation and development in different years during the last decade.

We gratefully acknowledge the open-data policies of NoRH, the ISAS/NASA satellite Yohkoh, the ESA/NASA satellite SOHO, the Big Bear and Kanzelhoehe Observatories, the National Astronomical Observatory of China, the NOAA's Space Environment Center GOES satellites, and their instrument teams whose data are used in this paper. We thank the referee, K. Tapping, for his important comments which helped to improve this paper.

References

Alissandrakis, C. E.; Lubyshev, B. I.; Smol'kov, G. Ia.; Krissinel', B. B.; Treskov, T. A.; Miller, V. G.; Kardapolova, N. N: 1992, *Solar Phys.* **142**, 341.

Alissandrakis, C. E.; Borgioli, F.; Chiuderi Drago, F.; Hagyard, M.; Shibasaki, K.: 1996, *Solar Phys.* **167**, 167.

Altyntsev, A. T.; Grechnev, V. V.; Kachev, L. E.; Lesovoi, S. V.; Mansyrev, M. I.; Molodyakov, S. A.; Platonov, A. V.; Saenko, I. I.; Smolkov, G. Y.; Sych, R. A.; Treskov, T. A.; Zandanov, V. G.; Esepkina, N. A.: 1994, *Astron. Astrophys.* **287**, 256.

Altyntsev, A. T.; Grechnev, V. V.; Zubkova, G. N.; Kardapolova, N. N.; Lesovoi, S. V.; Rosenraukh, Y. M.; Treskov, T. A.: 1995, *Astron. Astrophys.* **303**, 249.

Altyntsev, A. T.; Dutov, A. A.; Grechnev, V. V.; Konovalov, S. K.; Krissinel, B. B.; Lisysian, E. G.; Miller, V. G.; Rosenkraukh, Yu. M.; Smolkov, G. Ya.; Magun, A.: 1996a, *Solar Phys.* **168**, 145.

Altyntsev, A. T.; Grechnev, V. V.; Konovalov, S. K.; Lesovoi, S. V.; Lisysian, E. G.; Treskov, T. A.; Rosenraukh, Yu. M.; Magun, A.: 1996b, *ApJ.* **469**, 976.

Altyntsev, A. T.; Grechnev, V. V.; Hanaoka, Y.: 1998, *Solar Phys.* **178**, 575.

Altyntsev, A. T.; Grechnev, V. V.; Nakajima, H.; Fujiki, K.; Nishio, M.; Prosovetsky, D. V.: 1999, *Astron. Astrophys. Suppl. Ser.* **135**, 415.

Altyntsev, A. T.; Nakajima, H.; Takano, T.; Rudenko, G. V.: 2000, *Solar Phys.* **195**, 401.

Altyntsev, A. T.; Sych, R. A.; Grechnev, V. V.; Meshalkina, N. S.; Rudenko, G. V.: 2002, *Solar Phys.* **206**, 155.

Altyntsev, A. T.; Lesovoi, S. V.; Meshalkina, N. S.; Sych, R. A.; Yan, Yihua: 2003, *Astron. Astrophys. in press.*

Baars, J. W. M.; Hooghoudt, B. G.: 1974, *Astron. Astrophys.* **31**, 323.

Blinov, V. P.;, Blinova, R. V.; Vasin, V. I.; Derevyashkin, Y. V.; Dutov, A. A.; Krissinel, B. B.; Kuznetsova, S. M.: 1996, *Issledovaniya po geomagnetizmu, aeronomii i fizike Solntsa* **104**, 100 (*in Russian*).

Borovik, V. N.: 1994, *Lecture Notes in Physics, Advances in Solar Physics. Catania, Italy, 11-15 May, 1993.* **432**, 185.

Chiuderi Drago, F.: 1990, *Proc. of 117 IAU Colloq. Berlin and New York, Springer-Verlag*, 70.

Dulk, G. A.: 1985, *ARA&A* **23**, 169.

Felli, M.; Lang, K. R.; Willson, R. F. 1981, *ApJ.* **247**, 325.

Gelfreikh, G. B.; Pilyeva, N. A.; and Ryabov, B.I.: 1997, *Solar Phys.* **170**, 253.

Gopalswamy, N.; Shibasaki, K.; De Forest, C.E.; Bromage, B. J. I.; Del Zanna, G.: 1998, *in K. S. Balasubramanian, J. W. Harvey, and D. M. Rabin (eds.) ASP Conference Series.* **140**, 363.

Grechnev, V. V.: 2003, *Solar Phys.*, **213**, 103.

Krissinel, B. B.; Kuznetsova, S. M.; Maksimov, V. P.; Prosovetsky, D. V.; Grechnev, V. V.; Stepanov, A. P.; Shishko, L. F.: 2000, *PASJ* **52**, 909.

Kundu, M. R.: 1965, Solar Radio Astronomy. New York: Interscience Publication

Kundu, M. R.: 1985, *Solar Phys.* **100**, 491.

Kundu, M. R.; Alissandrakis, C. E.: 1984, *Solar Phys.* **94**, 249.

Landecker, T. L.; Dewdney, P. E.; Burgess, T. A. *et al.*: 2000, *Astron. Astrophys. Suppl.*, **144**, 509

Lesovoi, S.V.: 2001, *CESRA Workshop 2001 on Energy Conversion and Particle Acceleration in the Solar Corona.* http://www.copernicus.org/cesra/abstracts/cei7472.pdf.

Lubyshev B. I.; Prosovetskii D. V.; Treskov T. A.; Smolkov, G. Ya.; Krissinel, B. B.; Miller, V. G. 1996, *Izv. VUZov 'Radiofizika'*, **39**, 1466 (*in Russian*).

Maksimov, V. P.; and Bakunina, I. A.: 1991, *Soviet Astron.* **35**, 194.

Maksimov, V. P.; and Bakunina, I. A.: 1995, *Astron. Reports* **39**, 220.

Maksimov, V. P.; and Bakunina, I. A.: 1996, *Astron. Reports* **40**, 286.

Maksimov V. P.; and Nefedyev V. P.: 1991, *Solar Phys.* **136**, 335.

Maksimov V. P.; and Nefedyev V. P.: 1992, *Ann. Geophysicae* **10**, 354.

Maksimov, V. P.; Prosovetskii, D. V.; Krissinel, B. B.: 2001, *Astronomy Letters* **27**, 181.

Nakajima, H.; Nishio, M.; Enome, S.; Shibasaki, K.; Takano, T.; Hanaoka, Y.; Torii, C.; Sekiguchi, H.; Bushimata, T.; Kawashima, S.; Shinohara, N.; Irimajiri, Y.; Koshiishi, H.; Kosugi, T.; Shiomi, Y.; Sawa, M.; Kai, K.: 1994, *Proc. IEEE* **82(5)**, 705.

Napier, P. J.; Thompson, A. R.; and Ekers, R. D.: 1983, *Proc. IEEE* **71**, 1295.

Nefedyev, V. P.; Agalakov, B. V.; Smolkov, G. Ya.; Kardapolova, N. N.: 1993, *Annales Geophysical* **11**, No. 7, 614.

Ryabov, B. I.; and Maksimov, V. P.: 1999, *Structure and dynamics of the solar corona.* Ed. B.P. Philippov. Troitsk, IZMIRAN, 137 (*in Russian*).

Smolkov, G. Ia.; Pistolkors, A. A.; Treskov, T. A.; Krissinel, B. B.; Putilov, V. A.: 1986, *Astrophysics and Space Science* **119(1)**, 1.

Sych, R. A.; Uralov, A. M.; Korzhavin, A. N.: 1993, *Solar Phys.* **144**, 59.

Tapping, K. F.; Cameron, H. T.; Willis, A. G.: 2003, *Solar Phys., in press*

Uralov, A. M.; Sych, R. A.; Shchepkina, V. L.; Zubkova, G. N.; Smolkov, G. Ya.: 1998, *Solar Phys.* **183**, 359.

Uralov, A. M.; Grechnev, V. V.; Lesovoi, S. V.; Sych, R. A.; Kardapolova, N. N.; Smolkov, G. Ya.; Treskov, T. A.: 1998, *Solar Phys.* **178**, 557.

Uralov, A. M.; Lesovoi, S. V.; Zandanov, V. G.; Grechnev, V. V.: 2002 , *Solar Phys.* **208**, 69.

Zandanov, V. G.; and Lesovoi, S. V.: 1999, *Proceedings of the Nobeyama Symposium, held in Kiyosato, Japan, Oct. 27-30, 1998, Eds.: T. S. Bastian, N. Gopalswamy and K. Shibasaki* NRO Report **479**, 37.

Zandanov, V. G.; Altyntsev, A. T.; Lesovoi, S. V.: 1999, *Proceedings of the Nobeyama Symposium, held in Kiyosato, Japan, Oct. 27-30, 1998, Eds.: T. S. Bastian, N. Gopalswamy and K. Shibasaki* NRO Report **479**, 425.

Zheleznyakov, V.: 1970, *Radio Emission of the Sun and Planets. Pergamon Press, Oxford*

Zirin, H.; Baumert, B. M.; Hurford, G. J.: 1991, *ApJ* **370**, 779.

Zubkova, G. N.; Kardapolova, N. N.; Lubyshev, B. I.; Nefedyev, V. P.; Treskov, T. A.; Smolkov, G. Ya.; Sych, R. A.: 1990, *Astron. Nachr.* **311**, No. 4, 313.